J. Fluid Mech. (1985), *vol.* 161, *pp.* 513–532
Printed in Great Britain

Dynamics of vorticity fronts

By MELVIN E. STERN AND LAWRENCE J. PRATT†
Graduate School of Oceanography, University of Rhode Island, Kingston, Rhode Island 02881

(Received 25 June 1984 and in revised form 16 July 1985)

Vorticity fronts can form in a shear flow as the result of fast patches of fluid catching up with slower ones. This process and its consequences are studied in an inviscid two-dimensional model consisting of piecewise uniform-vorticity layers. Calculations using the method of contour dynamics for 'intrusive' initial states indicate that the leading edge of the front evolves into a robust structure whose propagation speed can be accounted for by a simple shock-joining theory. Behind the leading edge several different effects can occur depending upon the relative amplitude of the intrusion. These effects include lee-wave generation with possible wave breaking and folding of the front. A critical value of the frontal slope, above which wave breaking occurs, is suggested.

1. Introduction

A vorticity front, i.e. a surface separating regions of significantly different vorticities, can arise in several ways. A simple laboratory example occurs when the laminar flow from a round nozzle is increased from one steady discharge to another: the vorticity front forms in the intervening region separating the fast stream from the slower one (Stern & Vorapayev 1984). Dinkelacker & Langenheineken (1983) indicate that such coherent vorticity fronts can form in three-dimensional turbulent flows. We may also mention some important oceanic vorticity fronts, such as the inshore edge of the Gulf Stream in the Florida Strait (Stern 1985) as well as in the core further downstream (Hall & Bryden 1984).

A starting point for the discussion of the formation of fronts in a homogeneous fluid is provided by studies (Stern & Paldor 1983; Russell & Landahl 1984) of the evolution of large-amplitude and long-wave perturbations in a shear flow. In this asymptotic limit the downstream pressure gradients are neglected and (incompressible) 'shock' singularities form where fast fluid overtakes slow fluid. To proceed further Stern & Vorapayev (1984) proposed a shock-joining theory, across which the mass and vorticity fluxes are conserved, and due recognition is given to the stagnation pressure gradient at the shock front. A simple formula was thereby found for the propagation of these two-dimensional shocks in a shear flow, and the result was found to be consistent with the experimental results for laminar jets. Further support for this simple formula and picture is provided by the present study, which gives 'exact' solutions of the full Euler equations for the special case of piecewise uniform-vorticity flow (figure 1).

For the initial state shown in figure 1 (*a*) the lower layer, having unit non-dimensional vorticity, extends from $x = -\infty$ to $x = +\infty$, and $L(x, t)$ denotes the local non-dimensional thickness in the y-direction. From $y = L$ to $y = \infty$ there is an irrotational layer of fluid, and $y = 0$ is a rigid slippery boundary. As $x \to +\infty$ $L(x, t)$ approaches

---

† Present address: Woods Hole Oceanographic Institution, Woods Hole, MA 02543.

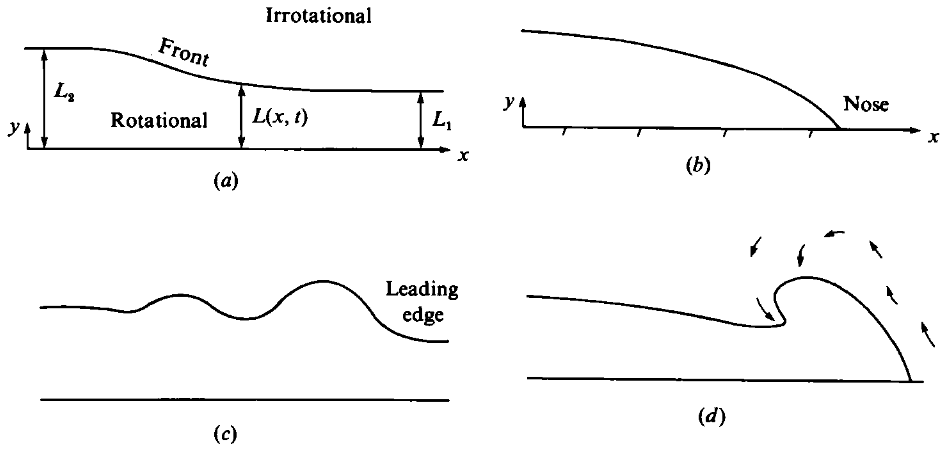

FIGURE 1. Schematic or uniform-vorticity layer below $y = L(x, t)$. (a) An initial state. (b) Initial state when $L_1 = 0$. (c) At a later time the front steepens and propagates. (d) The front of the nose steepens at a later time, 'backward' wave breaking occurs, and irrotational fluid is entrained.

the constant value L_1, $L \rightarrow L_2$ as $x \rightarrow -\infty$, and we suppose that initially L varies slowly in between. The extreme value $L_1/L_2 = 0$ (figure 1b) yields a blunt nose and is of particular interest because it corresponds to the frontal intrusion of a fluid of one vorticity into a fluid of completely different vorticity (cf. Stern & Vorapayev 1984). But for all values of $L_1/L_2 < 1$ (figure 1c) we shall show that a leading edge may be defined for the intrusion which propagates in a stable and well-defined way.

The piecewise uniform-vorticity model enables us to eliminate the y-dimension from the Euler equations (§2), and thereby reduces the problem to an integro-differential equation for $L(x, t)$ (Zabusky & Overman 1981). When $\partial L/\partial x \ll 1$ this reduces to the previously mentioned long-wave equations, according to which each L propagates with a speed L, so that the gently sloping regions in either figure 1(a) or 1(b) will steepen with time. The numerical solutions for the full equations will show that the short-wave effects cause the leading edge of the intrusion to equilibrate, as *assumed* in the previously mentioned shock-joining theory, and to propagate approximately at the speed $u_* = \frac{1}{2}(L_1 + L_2)$. One new qualitative effect appearing behind the leading edge (figure 1d) shows the 'backwards' breaking of the frontal intrusion followed by the engulfment of irrotational fluid. This effect is similar to that found by Pullin (1981) for the case of x-periodic disturbances on an interface. Figure 1(a) differs from Pullin's model insofar as the mean interface heights are different at $x = \pm\infty$. We shall also show that a kind of lee wave (figure 1b) develops behind the leading edge when L_1/L_2 is not too small, whereas when $L_1/L_2 \ll 1$ the waves behind the leading edge break as in figure 1(d). Wave breaking is said to occur first when $L(x, t)$ becomes multi-valued, and the term 'folding', 'overturning' and engulfment of irrotational fluid are used to describe the subsequent events. The critical value of $\partial L/\partial x$ for wave breaking is discussed in §6.

2. Contour dynamical equations

In a piecewise uniform-vorticity flow (figure 1) the non-dimensional stream function satisfies $\nabla^2\psi = 1$ for $L(x, t) > y > 0$; $\nabla^2\psi = 0$ for $\infty > y > L$; and $\psi(x, \infty, t) = 0$ and $\psi(x, 0, t) = \text{constant}$. The latter boundary condition can be satisfied by introducing image vortices in the solution of Poisson's equation, and thus we get

$$4\pi\psi(x,y,t) = \int \mathrm{d}\xi \int_0^{L(\xi,t)} \mathrm{d}\eta \ln \frac{(x-\xi)^2+(y-\eta)^2}{(x-\xi)^2+(y+\eta)^2}. \tag{1}$$

When $L_1 = 0$, a nose point $x_0(t)$ exists such that $L(x_0(t),t) = 0$ and the ξ-integration extends from $-\infty$ to $\xi = x_0(t)$.

It is easy to show that (1) (and (2)–(3) below) is valid even if L is a multi-valued function of x, in which case (L,x) are expressed as single-valued functions of distance measured along the curve.

For any point (L,x) on the curve the Lagrangian velocity components $v = \partial\psi/\partial x$, $u = -\partial\psi/\partial y$ are:

$$v = \mathrm{d}L/\mathrm{d}t, \tag{2}$$

$$u = \mathrm{d}x/\mathrm{d}t, \tag{3}$$

where

$$u = \frac{1}{4\pi}\int_{-\infty}^{\infty} \mathrm{d}\xi \ln \frac{\{(x-\xi)^2+[L(x,t)-L(\xi,t)]^2\}\{(x-\xi)^2+[L(x,t)+L(\xi,t)]^2\}}{[(x-\xi)^2+L^2(x,t)]^2}, \tag{4}$$

$$v = \frac{1}{4\pi}\int_{-\infty}^{\infty} \mathrm{d}\xi \frac{\partial L(\xi,t)}{\partial \xi} \ln \frac{(x-\xi)^2+[L(x,t)-L(\xi,t)]^2}{(x-\xi)^2+[L(x,t)+L(\xi,t)]^2}, \tag{5a}$$

$$= \frac{1}{4\pi}\int_{-\infty}^{+\infty} \mathrm{d}\xi \frac{\partial L(x-\xi,t)}{\partial x} \ln \frac{\xi^2+[L(x,t)-L(x-\xi,t)]^2}{\xi^2+[L(x,t)+L(x-\xi,t)]^2}, \tag{5b}$$

and where

$$L(-\infty,t) = L_2, \tag{6}$$

$$L(\infty,t) = L_1. \tag{7a}$$

When $L_1 = 0$, (7*a*) is replaced by

$$L(x_0(t),t) = 0, \tag{7b}$$

and the upper limit (∞) in (4) and (5*a*) is replaced by the nose position $x_0(t)$. These are the integro–differential equations for the evolution of $L(x,t)$.

3. Limiting and special cases

3.1. *Periodic disturbances of small amplitude*

It is easy to show from the results of §2 that infinitesimal amplitude perturbations of an undisturbed interface at $L = 1$ (i.e. $L_1 = L_2 = 1$) propagate with speed

$$c = \frac{1}{2k}(1-\mathrm{e}^{-2k}), \tag{8}$$

where k is the wavenumber (also see Pullin 1981). These waves propagating in the same horizontal direction as the shear flow have the 'long-wave' limit ($k \ll 1$)

$$c = 1-k+\dots, \tag{9}$$

while the short-wave limit ($k \gg 1$) gives

$$c = \frac{1}{2|k|}. \tag{10}$$

3.2. *The nonlinear, long-wave limit*

Suppose that $O(1)$ variations in L occur slowly in x (and t); i.e. assume L is a function of ϵx where $\epsilon \rightarrow 0$. We may then replace $\partial L(x-\xi)/\partial x$ by $(\partial L/\partial x)(1+O(\epsilon))$; and likewise $\xi^2+\{L(x,t)-L(x-\xi,t)\}^2 \simeq \xi^2$, so that the asymptotic value of (5a) is

$$v = \frac{1}{4\pi}\frac{\partial L}{\partial x}\int_{-\infty}^{\infty} \mathrm{d}\xi \ln\frac{\xi^2}{\xi^2+4L^2(x,t)} = -L\frac{\partial L}{\partial x}. \tag{11}$$

The corresponding long-wave limit of u must also have a leading term, which vanishes as $\partial L/\partial x \rightarrow 0$, as may be verified by using $L(x,t)$ = constant in (4) and by manipulating the integrals. Therefore the exact kinematical boundary condition

$$v = \frac{\mathrm{d}L}{\mathrm{d}t} = \frac{\partial L}{\partial t}+u\frac{\partial L}{\partial x} \tag{12}$$

reduces to

$$\frac{\partial L}{\partial t}+L\frac{\partial L}{\partial x} = 0 \tag{13}$$

in the $\epsilon \rightarrow 0$ limit, implying that $\partial L/\partial t$ is small to the same order as $\partial L/\partial x$.

This simple result (13) can be readily obtained using the Euler equations without going through the formidable route of (2)–(5) (see Stern & Paldor 1983 for the procedure). It implies that an observer moving with a fixed large value of L will overtake one moving with a smaller L; or that negative $\partial L/\partial x$ will steepen with time and lead to a singularity at $t = -[\min \partial L/\partial x]^{-1}$.

3.3. *Weakly nonlinear limit*

Reconsider disturbances having small ($O(\epsilon)$) amplitude and small ($O(k)$) spatial variation about $L = 1$. The nonlinear equation (13) suggests the wave speed is $1+O(\epsilon)$, while the linear and weakly dispersive relation (9) gives a speed $1+O(k)$. These results suggest that a balance between nonlinear and dispersive effects can be achieved by allowing the spatial variation of the front to be as small as the amplitude; $k = O(\epsilon)$. Such a balance leads to the Benjamin–Ono equation (Benjamin 1967):

$$\frac{\partial L}{\partial t}+L\frac{\partial L}{\partial x}-\mathscr{F}\left(\frac{\partial L}{\partial x}\right) = 0, \tag{14}$$

where
$$\mathscr{F}(g(x)) = \frac{1}{2\pi}\int_{-\infty}^{\infty}\mathrm{d}k\left\{|k|\,\mathrm{e}^{-\mathrm{i}kx}\int_{-\infty}^{\infty}\mathrm{d}x'\,g(x')\,\mathrm{e}^{\mathrm{i}kx'}\right\}.$$

(The details of the derivation appear in Appendix A.) As shown by Benjamin (1967), (14) admits progressive wave solutions as well as a solitary wave. Reference is also made to the soliton solutions obtained by Meiss & Pereira (1978) and Chen, Lee & Pereira (1979).

3.4. *The steep-slope limit*

Now consider the case where L *increases* rapidly ($\partial L/\partial x = O(\epsilon^{-1})$) from one constant value L_2, to another constant L_1 in a short interval $x \pm O(\epsilon)$. This is a 'backward'-facing step, whereas if L decreases rapidly (as in figure 2) we have a 'forward'-facing step. An asymptotic theory for the large ($1/\epsilon$) value of $\partial L/\partial t$ will be developed in order to ascertain whether or not max $\partial L/\partial x$ continues to increase and wave breaking occurs later in time. With the upper limits set equal to $+\infty$ in (4)–(5a) we obtain the leading ($\epsilon = 0$) terms in $u(L), v(L)$ as follows. Break the x-integration interval into three parts, the middle one of width $\epsilon \rightarrow 0$ being the dominant contributor to $v(L)$ (in $L_2 < L < L_1$), but a negligible contributor to $u(L)$. The value of the latter (in

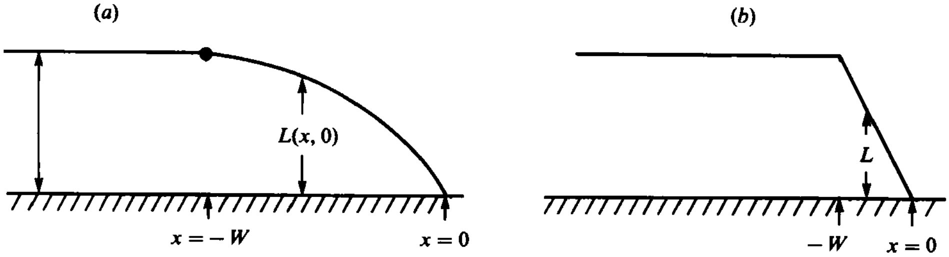

FIGURE 2. Sketch of two initial conditions used. (*a*) Parabolic nose for $-W < x < 0$. (*b*) Linear nose for $-W < x < 0$.

$L_2 < L < L_1$) is therefore obtained from the two adjacent integration intervals, in one of which $L = L_2$, and in the other $L = L_1$. This gives

$$4\pi u(L)$$
$$= \int_{-\infty}^{0} \mathrm{d}\xi \ln \frac{[\xi^2+(L-L_2)^2][\xi+(L+L_2)^2]}{(\xi^2+L^2)^2} + \int_{0}^{\infty} \mathrm{d}\xi \ln \frac{[\xi^2+(L_1-L)^2][\xi^2+(L_1+L)^2]}{(\xi^2+L^2)^2},$$

and therefore $$u(L) = \tfrac{1}{2}(L_1-L) \quad \text{for} \quad (L_2 < L < L_1). \tag{15}$$

Since $u(L_2) > u(L_1)$ we see that the closely separated points $x(L_2)$, $x(L_1)$ tend to *converge* with time. For a forward-facing step ($L_2 > L > L_1$), on the other hand, we obtain $u(L) = \frac{1}{2}(L_2-L)$, which shows that $x(L_2), x(L_1)$ *diverge* with time, and that *a 'forward'-facing step never breaks*. Thus the forward steepening implied by long-wave theory (13) always equilibrates at a finite $\partial L(x,t)/\partial x$, and the steepening that occurs on short spatial scales is opposite in sense to that predicted by the long-wave equation (13).

Returning to the backward-facing step (15) we find that the corresponding normal velocities

$$2\pi v(L) = (L-L_2)\ln(L-L_2)+(L_1-L)\ln(L_1-L)$$
$$-(L+L_1)\ln(L+L_1)+(L+L_2)\ln(L+L_2) \tag{16}$$

are $O(1)$ functions in $L_2 < L < L_1$. Therefore the asymptotic (steep-slope, short-time) version of (12) is $\partial L/\partial t + u\,\partial L/\partial x = 0$, or

$$\frac{\partial L}{\partial t} + \tfrac{1}{2}(L_1-L)\frac{\partial L}{\partial x} = 0. \tag{17}$$

This implies that each value of L (in the steeply sloping region) propagates with constant speed $\frac{1}{2}(L_1-L) > 0$, and consequently $L(x,t)$ will become multi-valued, or wave breaking and overturning will occur, in the (short) time

$$t_{\mathrm{B}} = \frac{2}{\max(\partial L(x,0)/\partial x)} \tag{18}$$

after the initial condition.

3.5. *Miscellaneous observations on the case* $L_1 = 0$

When $L_1 = 0$, (4) together with the nose condition (7*b*) give an expression for the propagation speed of the nose:

$$U_* = \frac{1}{2\pi}\int_{-\infty}^{0} \mathrm{d}\xi \ln \frac{\xi^2+L^2(\xi,t)}{\xi^2}. \tag{19}$$

If $L(-\infty, t) = 1$, and $L(x,t)$ decreases monotonically to the nose (as in figure 2) then the above expression gives

$$U_* \leqslant \tfrac{1}{2}. \tag{20}$$

The equality sign holds, and the nose speed equals $\frac{1}{2}$, when $L = 1$ everywhere except at the nose (where it decreases rapidly to zero). This $L(x,t)$ might be regarded as a solution of the 'long-wave equations' (§3.2) supplemented by our shock-joining condition. This solution with (20) conserves mass in the high-vorticity layer, and it is also consistent with the qualitative idea of §3.4 pertaining to the lack of wavebreaking in forward-facing steps. The first indication of the limitations of this 'solution' is revealed by (5*a*) which requires that if L decreases monotonically with x then $v > 0$, and thus L cannot remain monotonically decreasing as implied above. A useful explicit calculation of $v(x,0)$ for the initial $L(x,0)$ shown in figure 2(*b*) is

$$4\pi v = \int_0^1 \mathrm{d}z \ln \frac{W^2(\lambda - z)^2 + (1+z)^2}{W^2(\lambda - z)^2 + (1-z)^2}, \tag{21a}$$

$$\lambda \equiv -\frac{x}{W} \geqslant 1,$$

and for large negative x this becomes

$$v \rightarrow \frac{1}{2\pi x^2} \quad (x \ll -W). \tag{21b}$$

For $W = 0$ the corresponding horizontal velocity is

$$4\pi u = \int_{-\infty}^{-x} \mathrm{d}z \ln \frac{z^2}{z^2+1} \frac{z^2+4}{z^2+1} \rightarrow -|2\pi x|^{-1}. \tag{22}$$

Equation (21*b*) shows that positive v occur in the region of constant L [whereas the long-wave theory (13) implies that $v = 0$ here] so that the temporal evolution of both figures 2(*a*) and (*b*) may be expected to develop a maximum $L(x,t) > 1$, with positive $\partial L/\partial x$ behind the nose of the front. This is the first indication of important qualitative effects (overturning) which are entirely missed by the long-wave–shock-joining theory.

4. Numerical method

The numerical method used to integrate (2)–(5) is essentially that of Zabusky, Overman and co-workers (see Zabusky & Overman 1981 and references contained therein). Briefly put, the method is based on a Lagrangian scheme in which tagged fluid particles on the front are followed. The integrals (4) and (5) are evaluated using the trapezoidal rule, with tagged particles marking the endpoints of the trapezoids, and the particle motion is computed by integrating (2) and (3) using the Adams predictor–corrector method (Gear 1977). The novel features of our algorithm are due to the end conditions at the 'tails' and 'nose' point of the intrusion. In Appendix B, these modifications are described and a listing of the finite-difference equations is given. In all cases the number of tagged frontal particles is 160.

5. Results for the intrusive solution

We first describe the numerical results obtained using initial states of the forms shown in figure 2, with $L_1 = 0$, $L_2 = 1$. Results for this case are reproduced in a frame

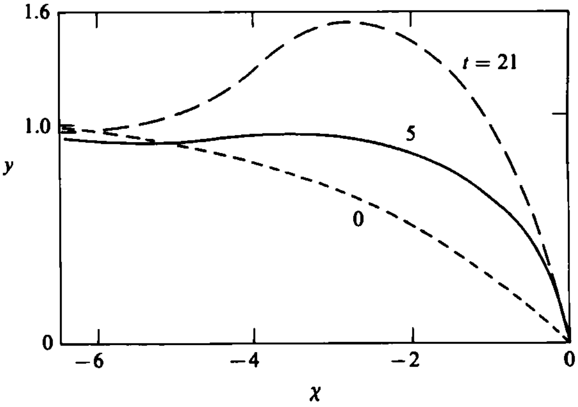

FIGURE 3. Evolution of parabolic nose with $W = 5.0$. The coordinate system moves with the nose speed.

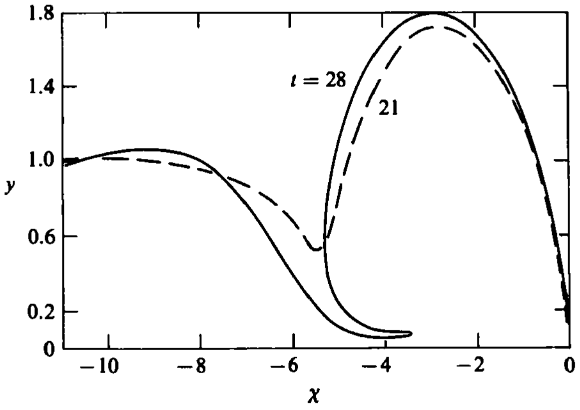

FIGURE 4. Continuation of figure 3 showing the front at $t = 21$ and $t = 28$.

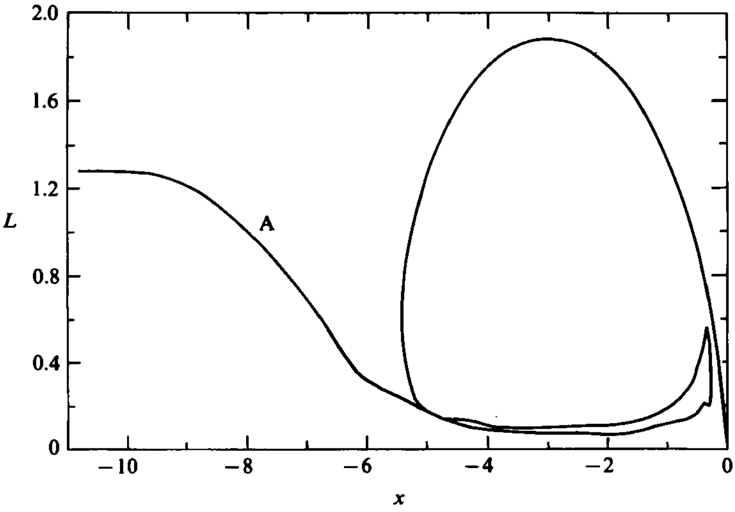

FIGURE 5. Continuation of figure 4 to $t = 36$. Note formation of multiply connected region and 'fission' near $x = -5$,

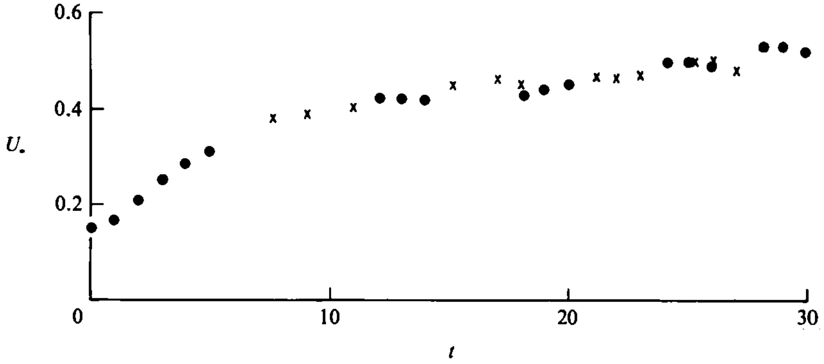

FIGURE 6. Nose velocity U_* as a function of time for figures 3–5. Smoothing and adding computation points (see text) was done only in between each sequence of 'dots' and crosses.

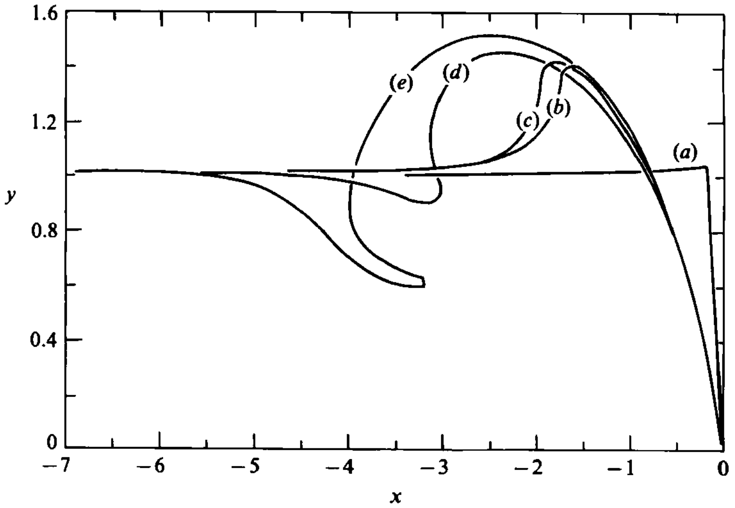

FIGURE 7. Evolution of linear profile (in figure 2*b*) for $W = 0.1$. (*a*) $t = 0.2$, (*b*) 3.0, (*c*) 4.4, (*d*) 6.0, (*e*) 9.0.

of reference moving with the nose speed U_*, and with the nose positioned at $x = 0$. First consider the initial condition (figure 2*a*)

$$L(x,0) = \begin{cases} 1 & (x \leqslant -5), \\ -\frac{1}{25}x(x+10) & (-5 < x < 0), \end{cases}$$

with the Lagrangian points distributed between $x = -8.0$ and $x = 0$. The steepening (figure 3) of the forward edge of the front from $t = 0$ to $t = 5.0$ is in qualitative accord with long-wave theory. Note that at $t = 5$ the nose speed (figure 6) is considerably less than the averaged velocity ($\frac{1}{2}$) within the lower layer at $x = -\infty$, and this difference accounts for the temporally increasing area bounded by the curves in figure 3. Also note that the slope of the leading edge of the front seems to reach a limiting value at $t = 21$. Figure 4 shows that behind the nose continuing steepening occurs with wave breaking ($\partial L/\partial x = +\infty$) at $t \cong 24$. At $t = 36$ (figure 5) we see the engulfment and entrainment of the irrotational fluid by the cyclonic nose vortex. Figure 6 suggests that the nose velocity eventually levels off at a value near $\frac{1}{2}$.

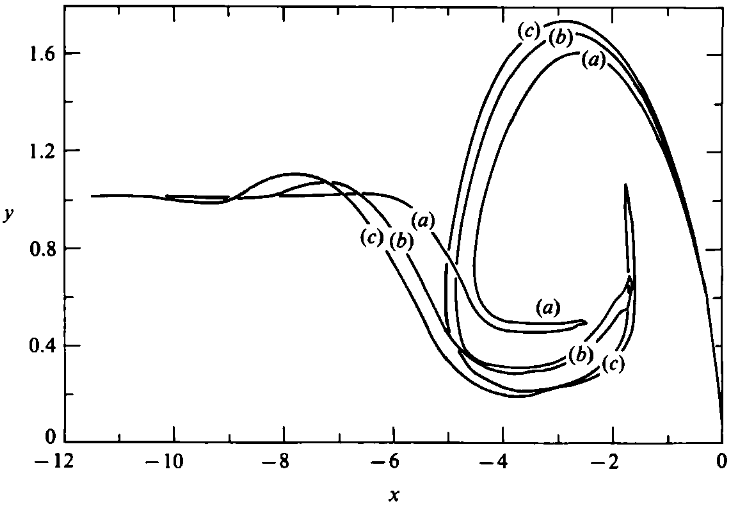

FIGURE 8. Continuation of figure 7 at (*a*) $t = 12$, (*b*) 15, (*c*) 19.

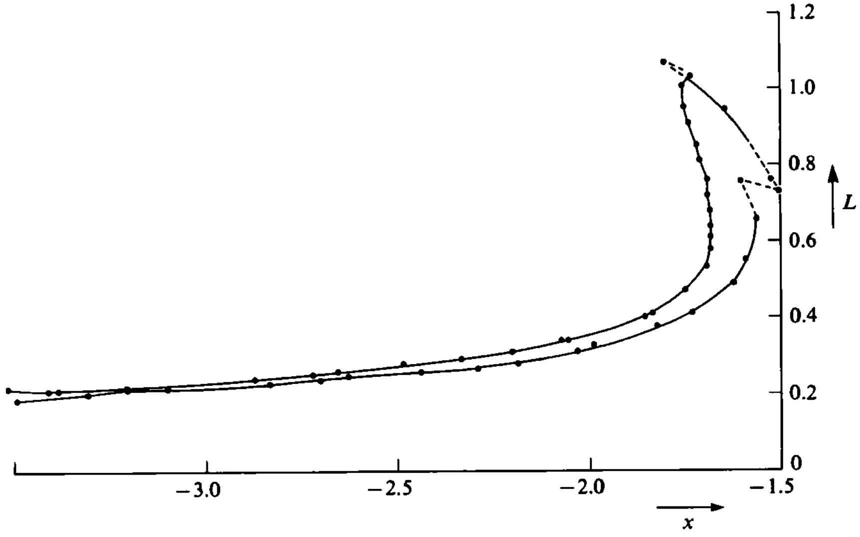

FIGURE 9. Enlarged view of $t = 19$ in figure 8, showing the onset of multi-connectedness and 'fission' at $x = -3.2$. The dashed portions of the front show regions of numerical uncertainty.

These results can be compared with those for a quite different initial condition (figure 2*b*) having much smaller initial scale: $W = 0.1$. The initial slope here is so steep that the asymptotic theory of §3.3 applies, and thus the magnitude of the nose slope *decreases* with time because $\partial L/\partial x$ is negative. The temporal evolution is shown in figures 7–9, and the nose speed in figure 10. Once again there is a temporal equilibration of the leading edge, and in order to compare this with the previous case we have plotted (figure 11) the frontal shapes at 'corresponding times', for which the nose speeds are approximately equal. Figure 11 suggests a similarity solution for the leading edge of the front with U_* as the relevant scaling parameter. In any case the qualitative behaviour of the leading edge, with regard to structure, coherence and

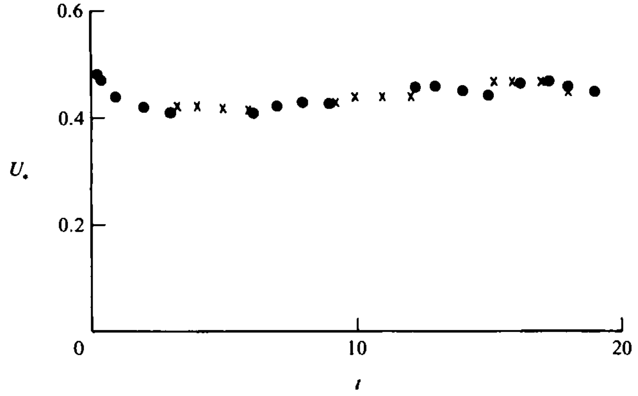

FIGURE 10. Nose speed for figures 7–9. Compare to figure 6.

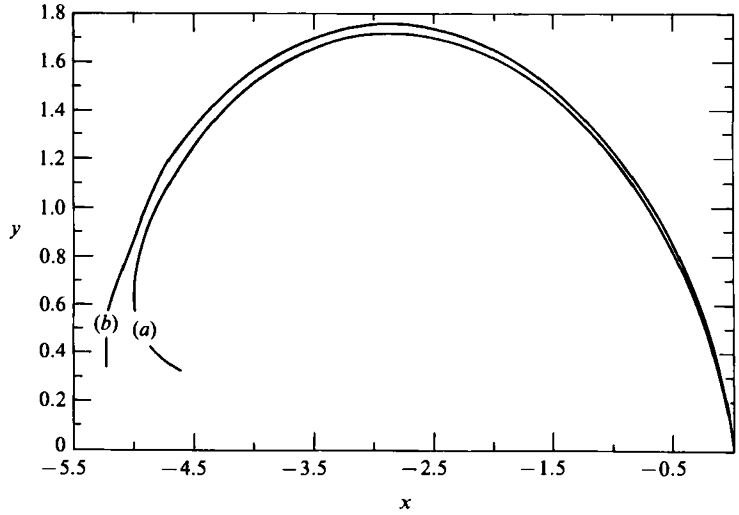

FIGURE 11. Comparison of the nose shapes for the two different numerical runs and values of t for which the two nose speeds are nearly equal (see text). 'Similarity' for the nose is suggested as well as 'robustness'.

robustness, is in accord with the implication of the simple long-wave–shock-joining theory. The importance of this lies in the fact that the latter theory is analytically tractable for the *three*-dimensional problem (see section VI of Stern & Paldor 1983), whereas the numerical method is not.

The time $t \cong 3.0$ of wave breaking in figure 7 is less than the corresponding time in the previous case because the initial width W is much smaller. But the subsequent engulfment and entrainment effects (figure 8) are qualitatively similar (to figure 5), and in both cases there are signs of a new negatively sloping front forming behind the nose vortex.

The calculations have been stopped at the indicated times because of the tendency for multi-connected regions to form, whereas a basic idea of inviscid theory seems to be that multiply connected regions cannot form at any t if the region is simply connected at $t = 0$. Implementation of the present algorithm becomes difficult when

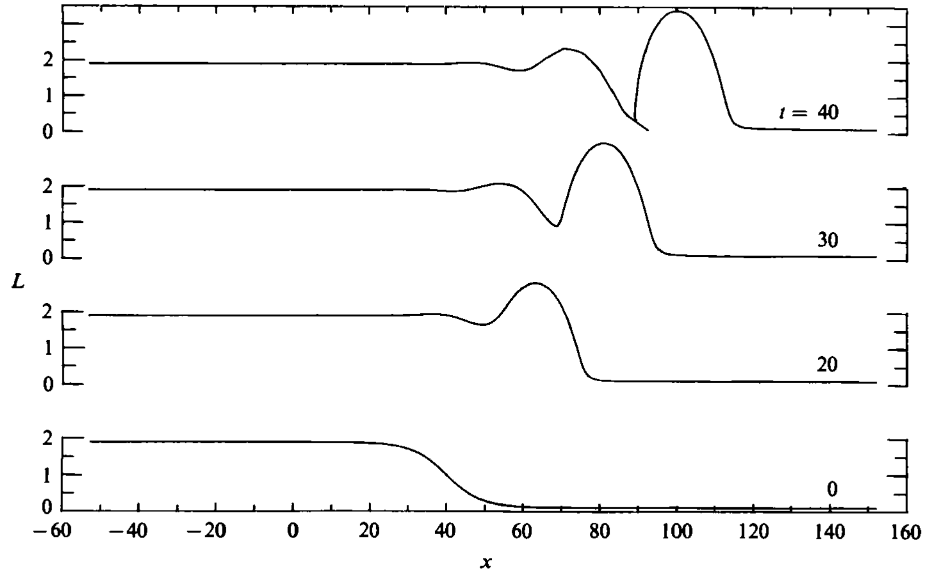

FIGURE 12. Time evolution of the case $L(x,0) = 1-a\tanh(0.2x)$ with $a = 0.9$.

grazing contact occurs (as in figure 9) between the line segment connecting points $(j, j+1)$ and the segment connecting $(k, k+1)$, where $j \neq k$. If the algorithm converges at such times (and if solution of the Euler equations exists) we require that the spacing between points be kept much less than the decreasing distance between points j and k. It is not known whether the grazing contact shown in figure 9 is the beginning of a real eddy fission, such as would occur without 'trauma' in a viscous fluid. Figure 9 at $x = -1.75$ reveals another and more common topological catastrophe, wherein two nearby segments intersect. This and the other jagged feature occur in regions of high front curvature where resolution problems become acute (Zabusky & Overman 1981). They can often be removed without noticeable effects elsewhere by deleting one point or by smoothing. As an example of the latter refer to figure 6, wherein the first set of dotted points are part of an integration extending to $t = 10$ with no smoothing. We then used as initial conditions the data at $t = 5$, with a few data points omitted and added as previously mentioned. The numerical calculation was then run, and the first part of the result is indicated by the first set of crosses. In this way we obtained overlapping sequences of results, from which we could ascertain the effects of the smoothing mentioned above. The most serious error was in the computation of the nose speed, as can be seen from the slight jagged appearance of the sets of data points in figure 6. Otherwise the effects of smoothing are believed to be inconsequential.

Next consider the case of finite L_1 as determined by the initial condition

$$L = 1-a\tanh(\tfrac{1}{5}x) \quad (0 \leqslant a \leqslant 1),$$

so that $L_2 = 1+a$ and $L_1 = 1-a$. Figure 12 shows the frontal evolution which results from the case $a = 0.9$. The frame of reference is now at rest and the intrusion or 'bore' moves from left to right. As before, the leading edge of the bore initially steepens $(0 \leqslant t \leqslant 20)$ and eventually reaches a state of quasi-equilibrium $(t = 30)$. But now secondary waves appear behind the leading edge before the wave breaking occurs at $t \cong 40$.

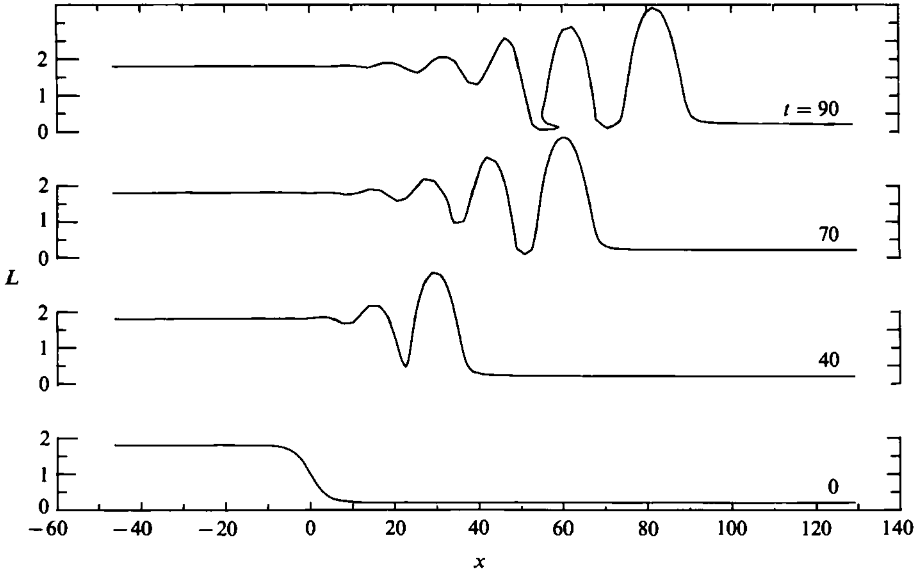

FIGURE 13. Same as figure 12 but with $a = 0.8$.

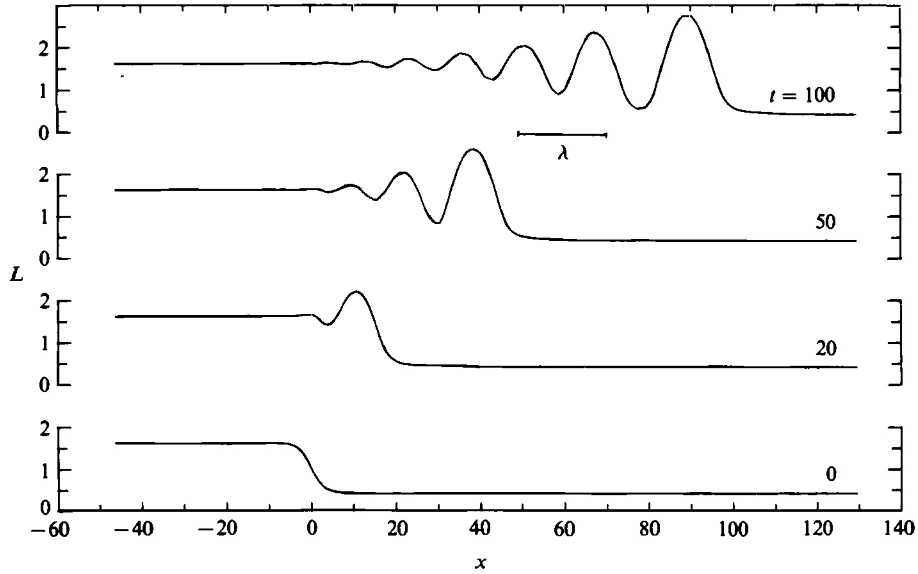

FIGURE 14. Same as figure 12 but with $a = 0.6$. The characteristic wavelength, computed from (8), has been indicated near the $t = 100$ profile.

Figure 13 shows a slightly smaller-amplitude ($a = 0.8$) case. Here the leading edge evolves as before but the secondary waves become more fully developed before overturning occurs (now at $t \cong 90$). Curiously, it is the second, rather than the first, wave that overturns.

Wave breaking is entirely absent in the case $a = 0.6$ (figure 14). Here the front evolves in the manner of the classical undular bore of surface gravity waves, with the excess mass carried by a train of undulations whose mean level is the level far

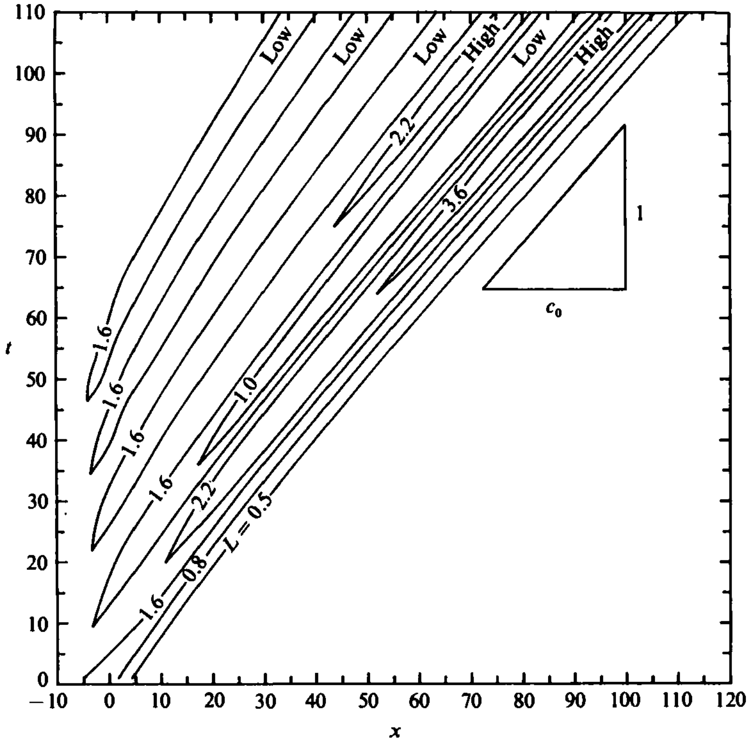

FIGURE 15. Plot of contours of uniform $L(x, t)$ as a function of x and t for the undular bore of figure 14.

upstream $L_2 = 1.6$. Figure 15 contains a characteristic plot showing the time–space path of equal values of L in the developing bore. This plot reveals a number of interesting features. First, the leading edge quickly equilibrates and propagates with speed $= 0.96$, which is approximately the average long-wave speed $\frac{1}{2}(L_1 + L_2) = 1.0$. (The leading-edge speeds for the case $a = 0.9$ and $a = 0.8$ are 0.95 and 1.05 respectively.) If this speed is substituted for c in (8) and the mean level $L = L_2$ is used, a characteristic wavelength $\lambda = 2\pi/k = 19.6$ is obtained. This length has been indicated in figure 14 and can be seen to be typical of the length of the undulations. Secondly, undulations following the leading edge also equilibrate and propagate with remarkably constant form at the speed of the leading edge, as revealed by the parallel lines of equal L in the upper right-hand part of figure 15. Finally, all new troughs and crests are created near the origin, as indicated by the position of the cusps in the $L = 1.6$ contours of figure 15. No propagation occurs to the left of the origin, a fact consistent with the non-negativity of the group velocity:

$$c_2 = \frac{\partial(kc)}{\partial k} = L\,\mathrm{e}^{-2L|k|} > 0.$$

The quasi-steady nature of the leading wave is further illustrated by the time evolution of the crest and trough height, labelled $L_{\max}$ and $L_{\min}$, as shown in figure 16. Both values experience rapid changes from $t = 0$ to $t = 50$, and then change more gradually with an eventual levelling off near the respective values $L_2 \pm 2a$ ($= 0.4$ and 2.6). Unfortunately, resolution problems begin to occur after $t = 100$ and further

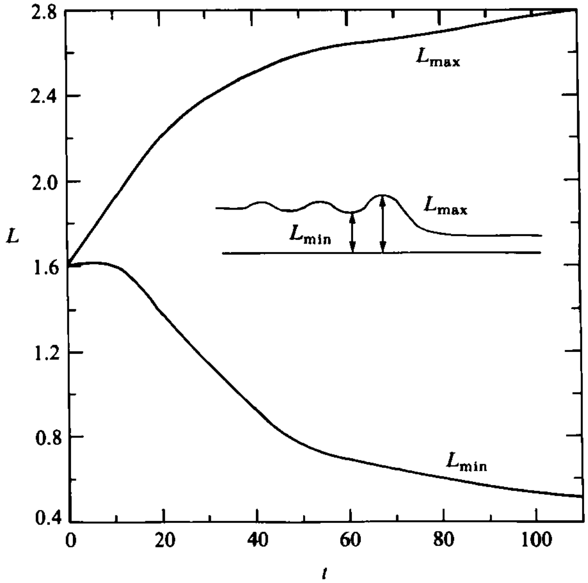

FIGURE 16. Elevation of the crest (L_{max}) and trough (L_{min}) of the first undulation in the bore of figure 14 as a function of time.

integration becomes unreliable. Nevertheless, one might ask whether some scaling law exists which relates the mean thickness L with the length λ and amplitude A of these waves. The answer to this question is unknown; however, we note that the steepness $A/(2\lambda)$ of the quasi-steady waves is 0.41 ± 0.05, a value that will reappear in our discussion of breaking waves.

6. The isolated-wave-breaking model

As indicated in §1 (see also §3.4) we want to isolate the wave-breaking effect by using a simpler model in which the initial L increases monotonically from L_2 to L_1 as x increases. Figure 17 shows the evolution of an initially piecewise linear $L(x,t)$ with $\max \partial L(x,0)/\partial x = 2$, and for visual convenience the reference frame here has been translated uniformly. The graph of each numerical solution up to the time of wave breaking is accompanied by the graph of (17), which consists of broken straight lines. We see that this simple solution quite nicely captures the overturning effect – although it fails to predict the decreasing minimum value of L, which is obviously important in the post-wave-breaking stage ($t = 2.0$).

Table 1 indicates the time of wave breaking for this initial $L(x,0)$ and for three other piecewise linear $L(x,0)$, which differ only in the value of the maximum slope. For $\max \partial L(x,0)/\partial x = 0.25$ no sign of wave breaking (or wave steepening) was observed up to $t = 6.0$, and we believe no wave breaking will occur at later time. Also computed was the case of a hyperbolic tangent $L(x,0)$ having the same $L(-\infty,0)$ and $L(+\infty,0)$ but with a maximum slope of 0.75. Wave breaking occurs for this and for the larger slope (4.0) indicated in table 1, but wave breaking does not occur when $\max \partial L(x,0)/\partial x$ is as small as 0.4. This is strong evidence that overturning in a piecewise uniform-vorticity flow occurs when $\max \partial L(x,0)/\partial x$ exceeds a critical value between 0.4 and 0.75. This compares reasonably well with Pullin's (1981) values

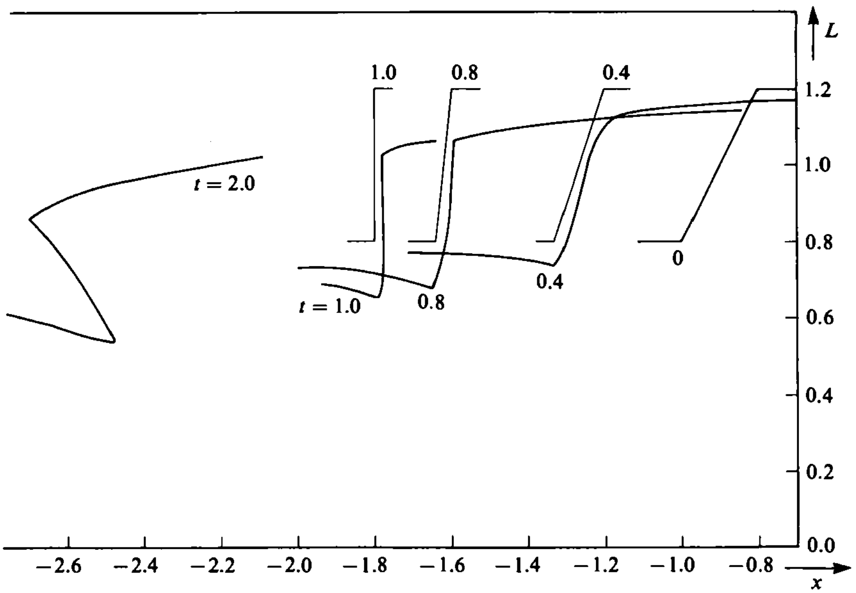

FIGURE 17. Temporal evolution of a 'backward'-facing step as indicated by the piecewise-linear L-profile at $t = 0$ (this extends to $x = \pm\infty$ without a nose). The coordinate system used in this figure (and only here) is uniformly translating at speed unity to avoid overlapping $L(x,t)$ profiles. The thin-lined profiles at $t = 0.4$, 0.8, 1.0 are based on the asymptotic steep-slope theory, whereas the heavy curves are more-exact numerical calculations. The theory predicts the time ($t = 1.0$) of backwards wave breaking quite well.

Initial shape of profile	$\max \partial L(x,0)/\partial x$	t_B or maximum time of computation
Piecewise linear	2.0 (figure 17)	1.0
	1.0	2.0
	0.75	2.4
	0.25	None ($t \leqslant 6.0$)
Hyperbolic tangent	4.0	0.5
	0.75	3.5
	0.4	None ($t \leqslant 20.0$)
$L(x,0) = 1+0.5(1+100x^2)^{-1}$	5 (figure 18)	1.5
$L(x,0) = 1+0.1(1+2500x^2)^{-1}$	5	1.5

TABLE 1. Time t_B of wave breaking

(0.29–0.39) obtained for sinusoidal disturbances. Note that the steepness of the equilibrated waves of figures 13 and 14 also fall within this range (see §5). The penultimate line in table 1 shows that an isolated bell-shaped disturbance (figure 18) can also break if its $\max \partial L/\partial x$ is sufficiently large. According to the asymptotic theory, the breaking time (18) should become independent of the distance of the lower boundary ($y = 0$) from the interface. To check this it was more convenient to keep the latter distance and $\max \partial L(x,0)/\partial x$ constant, while reducing the amplitude and x-scale by a factor of five, as indicated in the last line of table 1. The constancy of t_B verifies the similarity point at issue.

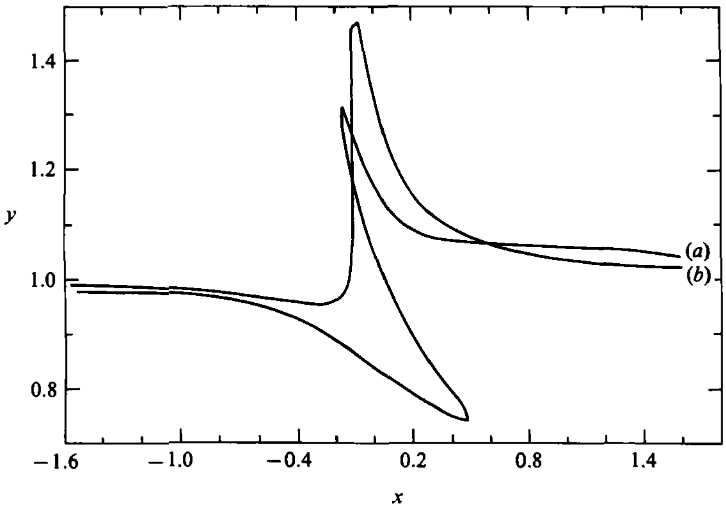

FIGURE 18. Initial $L(x,0) = 1+0.5(1+100x^2)^{-1}$. Profiles at $t = 1.5$ (curve *b*) and $t = 5.0$ (curve *a*).

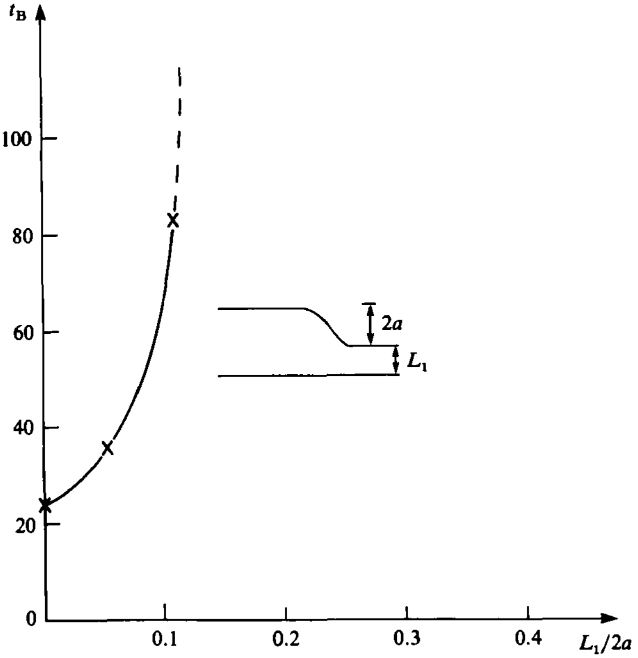

FIGURE 19. Breaking time t_B as a function of the amplitude factor $L_1/2a$ for the initial profile $L(x,0) = 1.0-a\tanh(0.2x)$. In addition to the three data points shown, the case $L_1/2a = \frac{1}{3}$ was computed with the result $t_B = \infty$.

It may be asked what 'forward'-facing disturbances lead to 'backward' wave breaking. Figure 19 shows breaking time as a function of the amplitude factor $L_1/2a$ for the forward-facing, hyperbolic-tangent disturbances exemplified in figures 12–14. The figure indicates that no breaking occurs (or, at least, that the breaking time becomes enormous) for values of $L_1/2a > 1.1$.

7. Conclusions

The numerical solutions of the two-dimensional Euler equations for a piecewise uniform-vorticity flow verify the simple and apparently general idea that a steeply sloping and robust leading (frontal) edge forms when a patch of fast-moving fluid catches up with a slower patch. Such a coherent feature might therefore be expected as an intermittent feature of large-Reynolds-number shear flow.

Also of interest are the effects which occur behind the leading edge as time advances. For large amplitudes (i.e. values of $L_1/2a < 0.11$) wavebreaking and engulfment of irrotational fluid occurs. For smaller amplitudes ($L_1/2a > 0.11$) a lee wave (reminiscent of the undular bore in gravity waves) develops behind the leading edge of the shear intrusion, and each successive wavelet tends to equilibrate in amplitude and preserve its form.

This work was supported by the Office of Naval Research under contract N00014-81-C-0062. The authors wish to thank Mrs L. Allen for typing the manuscript.

Appendix A. Weakly nonlinear limit

We document the case in which $L-1 = O(\epsilon)$ is as small as the spatial variation $\partial/\partial x \sim \epsilon$, so that $\partial L/\partial x = O(\epsilon^2)$ and thus (5*a*) reduces to

$$\begin{aligned} v &= \frac{1}{4\pi}\int_{-\infty}^{\infty} \mathrm{d}\xi\, \frac{\partial L}{\partial \xi} \ln \frac{(x-\xi)^2 + O(\epsilon^2)}{(x-\xi)^2 + 4L^2(x,t) + O(\epsilon^2)} \\ &= \frac{1}{4\pi}\int_{-\infty}^{\infty} \mathrm{d}\xi\, \frac{\partial L}{\partial \xi} \ln \frac{(x-\xi)^2}{(x-\xi)^2+4} + \frac{1}{4\pi}\int_{-\infty}^{\infty} \mathrm{d}\xi\, \frac{\partial L}{\partial \xi}\left[\ln \frac{(x-\xi)^2}{(x-\xi)^2+4L^2} + \ln\frac{(x-\xi)^2}{(x-\xi)^2+4}\right]. \end{aligned}$$

The neglected terms here are $O(\epsilon^4)$, and the integral is $O(\epsilon^3)$ since $L-1 = O(\epsilon)$. Therefore $\partial L/\partial \xi$ in the last integral may be replaced by $\partial L/\partial x$, whereupon we get

$$v = \frac{1}{4\pi}\int_{-\infty}^{\infty} \mathrm{d}\xi\, \frac{\partial L}{\partial \xi} \ln \frac{(x-\xi)^2}{(x-\xi)^2+4} - (L-1)\frac{\partial L}{\partial x} + O(\epsilon^4).$$

The first integral here is merely the contribution of linear theory, and its long-wave expansion is most readily obtained by inverting the Fourier transform of $\ln z^2/(z^2+4)$ as follows:

$$\begin{aligned} \frac{1}{4\pi}\int_{-\infty}^{\infty} \mathrm{d}\xi\, \frac{\partial L}{\partial \xi} \ln \frac{(x-\xi)^2}{(x-\xi)^2+4} &= -\frac{1}{4\pi}\int_{-\infty}^{\infty} \mathrm{d}k\, |k|^{-1}\, \mathrm{e}^{-\mathrm{i}kx}\,(1-\mathrm{e}^{-2|k|}) \int_{-\infty}^{\infty} \mathrm{d}\xi\, \frac{\partial L}{\partial \xi}\, \mathrm{e}^{\mathrm{i}k\xi} \\ &= -\frac{1}{2\pi}\int_{-\infty}^{\infty} \mathrm{d}k\, \mathrm{e}^{-\mathrm{i}kx}\,(1-|k|+O(k^2)) \int_{-\infty}^{\infty} \mathrm{d}\xi\, \frac{\partial L}{\partial \xi}\, \mathrm{e}^{\mathrm{i}k\xi} \\ &= -\frac{\partial L}{\partial x} + \mathscr{F}\left(\frac{\partial L}{\partial x}\right), \end{aligned}$$

where, following Benjamin (1967), we have introduced

$$\mathscr{F}(g(x)) = \frac{1}{2\pi}\int_{-\infty}^{\infty} \mathrm{d}k\, |k|\, \mathrm{e}^{-\mathrm{i}kx} \int_{-\infty}^{\infty} \mathrm{d}x'\, g(x')\, \mathrm{e}^{\mathrm{i}kx'}.$$

Thus we get

$$v = -L\frac{\partial L}{\partial x} + \mathscr{F}\left(\frac{\partial L}{\partial x}\right) + O(\epsilon^4).$$

Since u is of the same order as v, (13) again approximates to $v = \partial L/\partial t$, and we then obtain the Benjamin–Ono equation:

$$\frac{\partial L}{\partial t} + L\frac{\partial L}{\partial x} - \mathscr{F}\left(\frac{\partial L}{\partial x}\right) = 0.$$

Appendix B. Numerical method

Consider n material particles with initial positions $x_i(0)$ and $L_i(0)$, distributed along the front, with i increasing from left to right. The material points extend over the curved segment of the front and can be redistributed from time to time to maintain the required resolution.

First consider the case of non-zero L_1. Within the moving portion of the front, the integrals (4) and (5*a*) are evaluated using the trapezoidal rule, as in the algorithms of Zabusky & Overman (1981) or Pullin (1981). The novel feature of the present algorithm involves the special treatment of the tails $x < x_1$, and $x > x_n$. If x_1 and x_n are positioned sufficiently far from the primary region of frontal movement, then $\partial L/\partial x = 0$ in the tails and (5*a*) gives $v = 0$. Part of (4) can also be evaluated analytically at any x_i by substituting the constant value L_1 (or L_2) for $L(\xi, t)$, so that the contributions to u from the tails are

$$\begin{aligned} I_1 &= \frac{1}{4\pi}\int_{-\infty}^{x_1} \ln G_2(x_i, \xi)\, \mathrm{d}\xi \\ &= \pi(L_2 - L_i + |L_2 - L_i|) - R(x_i - x_1, |L_i - L_2|) \\ &\quad + 2R(x_i - x_1, L_i) - R(x_i - x_1, L_i + L_2), \end{aligned}$$

and

$$\begin{aligned} I_2 &= \frac{1}{4\pi}\int_{x_n}^{\infty} \ln G_2(x_i, \xi)\, \mathrm{d}\xi \\ &= \pi(L_1 - L_i + |L_1 - L_i|) + R(x_i - x_n, |L_i - L_1|) \\ &\quad - 2R(x_i - x_n, L_i) + R(x_i - x_n, L_i + L_1), \end{aligned}$$

where

$$G_2(x, \xi) = \frac{[(x-\xi)^2 + (L(x) - L(\xi))^2]\,[(x-\xi)^2 + (L(x) + L(\xi))^2]}{[(x-\xi)^2 + L^2(x)]^2}$$

and

$$\begin{aligned} R\hat{z}, a) &= \int_0^{\hat{z}} \ln(z^2 + a^2)\, \mathrm{d}z \\ &= \hat{z}\ln(\hat{z}^2 + a^2) - 2\hat{z} + 2|a|\tan^{-1}\frac{\hat{z}}{|a|}. \end{aligned}$$

The integrals (4) and (5*a*) were indented at the logarithmic singularities, and analytic approximations for the latter small intervals were obtained. In summary, the difference approximations to (4) and (5*a*) are

$$\begin{aligned} u_i \cong \frac{1}{4\pi}\Bigg\{\frac{1}{2} \sum_{\substack{j=2 \\ (j \neq i,\, i+1)}}^{n} & (x_j - x_{j-1}) \ln[G_2(x_i, x_j)\, G_2(x_i, x_{j-1})] \\ & + R(x_{i+1} - x_i, 2L_i) + R(x_i - x_{i-1}, 2L_i) - 2(x_{i+1} - x_{i-1}) \end{aligned}$$

$$
\begin{aligned}
&-2R(x_{i+1}-x_i, L_i)-2R(x_i-x_{i-1}, L_i)\\
&+(x_{i+1}-x_i)\ln[(x_{i+1}-x_i)^2+(L_{i+1}-L_i)^2]\\
&\left.+(x_i-x_{i-1})\ln[(x_i-x_{i-1})^2+(L_i-L_{i-1})^2]\right\}+I_1+I_2,
\end{aligned}
\qquad \text{(B 1)}
$$

$$
\begin{aligned}
v_i \cong \frac{1}{4\pi}\Bigg\{\frac{1}{2}\sum_{\substack{j=2\\(j\neq i,\, i+1)}}^{n} &(L_j-L_{j-1})\ln[G_1(x_i, x_j)\, G_1(x_i, x_{j-1})]\\
&-\tfrac{1}{2}(L_{i+1}-L_{i-1})\ln[(x_{i+1}-x_i)^2+(L_{i+1}+L_i)^2][(x_i-x_{i-1})^2+(L_i+L_{i-1})^2]\\
&+(L_{i+1}-L_i)\ln[(x_{i+1}-x_i)^2+(L_{i+1}-L_i)^2]-2(L_{i+1}-L_{i-1})\\
&+(L_i-L_{i-1})\ln[(x_i-x_{i-1})^2+(L_i-L_{i-1})^2]\Bigg\},
\end{aligned}
\qquad \text{(B 2)}
$$

where
$$G_1(x, \xi)=\frac{(x-\xi)^2+(L(x)-L(\xi))^2}{(x-\xi)^2+(L(x)+L(\xi))^2}.$$

When $L_1=0$, x_n is chosen to coincide with the nose (i.e. $L(x_n)=0$). The ξ-integration is then carried out from $-\infty$ to x_n and the contribution from the right-hand tail $x>x_n$ in (B 1) is absent. Also it is advantageous to carry out the computation in a frame of reference moving at the nose speed U_*. The latter is effected by subtracting from (B 1) the difference approximation to (19):

$$
\begin{aligned}
U_* \cong \frac{1}{4\pi}\Bigg\{\sum_{j=2}^{n}(x_j-x_{j-1})\ln&\left[\frac{(x_j^2+L_j^2)(x_{j-1}^2+L_{j-1}^2)}{x_j^2\, x_{j-1}^2}\right]\\
&+2\pi-2[R(-x_1, L_2)-R(-x_1, 0)]\Bigg\}.
\end{aligned}
\qquad \text{(B 3)}
$$

The motion of the frontal particles is computed from (2) and (3) using a version of the Adams predictor–corrector method due to Gear (1971).

REFERENCES

BENJAMIN, T. B. 1967 Internal waves of permanent form in fluids of great depths. *J. Fluid Mech.* **29**, 559.

CHEN, H. H., LEE, Y. C. & PEREIRA, N. R. 1979 Algebraic internal wave solitons and the integrable Calogero–Moser–Sutherland N-body problem. *Phys. Fluids* **22**, 187.

DINKELACKER, A. & LANGENHEINEKEN, TH. 1983 Relations between wall pressure fluctuations and velocity fluctuations in turbulent flow. In *Structure of Complex Turbulent Shear Flow* (ed. R. Dumas & L. Fulachier). Springer-Verlag.

GEAR, C. W. 1971 *Numerical Initial Value Problems in Ordinary Differential Equations.* Prentice-Hall.

HALL, M. M. & BRYDEN, H. 1984 Four profiles across the Gulf Stream at 68° west (In preparation).

MEISS, J. D. & PEREIRA, N. R. 1978 Internal wave solitons. *Phys. Fluids* **21**, 700.

PULLIN, D. I. 1981 The nonlinear behaviour of a constant vorticity layer at a wall. *J. Fluid Mech.* **108**, 401–421.

RUSSELL, J. M. & LANDAHL, M. T. 1984 The evolution of a flat eddy near a wall in an inviscid shear flow. *Phys. Fluids* **27**, 557.

SAUNDERS, P. 1971 Development of a warm core ring. *Deep-Sea Res.* **18**, 1207.

STERN, M. E. 1985 Lateral wave breaking and shingle formation in large scale shear flow. *J. Phys. Oceanogr.* **15**, 1274.

STERN, M. E. & PALDOR, N. 1983 Large amplitude long waves in a shear flow. *Phys. Fluids* **26**, 906.

STERN, M. E. & VORAPAYEV, S. I. 1984 Formation of vorticity fronts in a shear flow. *Phys. Fluids* **27**, 848.

ZABUSKY, N. J. & OVERMAN, E. A. 1981 Regularization of contour dynamical algorithms. *J. Comp. Phys.* **52**, 357.